Disks of Galaxies : Kinematics, Dynamics and Perturbations
ASP Conference Series, Vol. iii, 2002
E. Athanassoula & A. Bosma, eds.

On the Spiral Structure of NGC 2915

Frédéric S. Masset

Service d'Astrophysique, CE-Saclay, 91191 Gif/Yvette Cedex, France

Martin Bureau

Columbia Astrophysics Laboratory, 550 West, 120th Street, 1027 Pupin Hall, Mail Code 5247, New York NY 10027, USA

Abstract. The galaxy NGC 2915 is a blue compact dwarf galaxy embedded in a very extended HI disk. This disk exhibits a grand-design two-armed spiral structure, as well as a central bar-like structure. We attempt to model this HI disk using column density and kinematics constraints provided by radio observations, in order to find a plausible excitation source for the spiral structure. Our models show that the spiral structure can be accounted for either by an unseen bar or a triaxial halo, and that the former leads to better fits with observations than the latter.

1. Introduction and observational characteristics

NGC 2915 is a weak BCD galaxy, at a distance $D = 5.3 \pm 1.6$ Mpc (Meurer et al. 1994), with radio properties rather unexpected: it has a very extended HI disk (which extends up to five times its Holmberg radius), in which a central bar-like structure and an outer grand-design two-armed spiral can be observed (Meurer et al. 1996, hereafter MCBF). The total mass to blue light ratio of this galaxy is $\mathcal{M}_T/L_B = 76$, which makes NGC 2915 one of the darkest disk galaxies known (MCBF). Bureau et al. (1999) have made a comprehensive list of possible mechanisms which could account for the bar/spiral structure of the HI disk of this galaxy. The purpose of this work is to investigate whether this structure could be the response to an external forcing by a rotating potential (which is presumably due to a triaxial halo or bulge or to a central bar, or a mixture of those). This is done by running a simple hydrodynamics code, exploring the parameter space so as to match the observations. We first present the relevant parameters and give suitable observational constraints. We then give a brief description of the code used for the modeling, and we outline the main results of our simulations. Other models have been attempted in which the possibility that the HI disk of NGC 2915 is more massive than what can be inferred from the HI column density, and for which the spiral structure could be due to instabilities such as the SWING. The results will be presented elsewhere (Masset & Bureau, in prep.).

The circular velocity and velocity dispersion of NGC 2915 are represented at Fig. 1. Hereafter we assume a distance $D = 5.3$ Mpc for NGC 2915. The rotation curve shows a rise up to $R = 5$ kpc, where it reaches a plateau of about

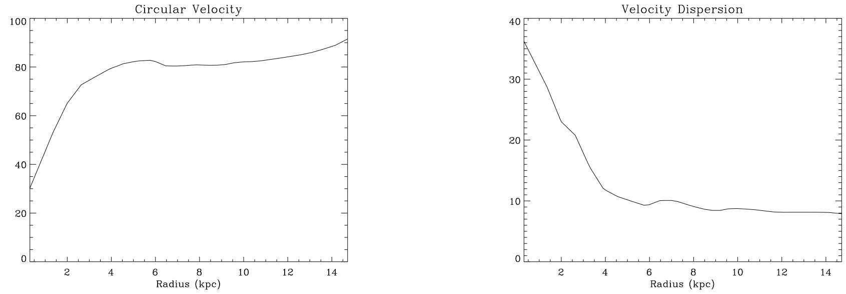

Figure 1. These diagrams represent the circular velocity (left) and velocity dispersion (right) as a function of distance to the disk center, in km/s. The circular velocity is corrected from the asymmetric drift.

$V_c = 80$ km/s. This circular velocity is corrected from the asymmetric drift, using the velocity dispersion shown in Fig. 1. Note that beam smearing effects tend to overestimate the velocity dispersion in the central regions, and that the circular velocity may be over-corrected (i.e., underestimated) in the central parts (the innermost 2 kpc). The Toomre Q parameter that can be estimated from this data set has a high value everywhere in the disk, with a minimum of ~ 6 for $r \sim 6$ kpc. As this value is very high, instabilities due to self-gravity effects (such as the SWING mechanism) are impossible if one assumes that the observed HI column density accounts for the disk mass of NGC 2915. Therefore we study the response of this disk to an external perturbing potential.

2. Disk response to a rotating non-axisymmetric forcing potential

One needs to identify the relevant constraints provided by the observations, and the parameters one can adjust so that the model matches the observation. The constraints are provided by the successive moments of the observational data cube (i.e. the column density map, the velocity map, the velocity dispersion).

2.1. Constraint from the column density map

Although the disk response in the case of NGC 2915 is non-linear, it is instructive to have a look at the dispersion relationship for an m-folded density wave in a thin isothermal disk of sound speed c_s, in the WKB limit, which reads:

$$m^2(\Omega - \Omega_p)^2 = \kappa^2 - 2\pi G\Sigma|k| + k^2c_s^2 \tag{1}$$

where $k^2 = m^2/r^2 + k_r^2$, and where k_r is the radial wavevector, Ω_p is the wave pattern frequency, Ω is the circular velocity, κ is the epicyclic frequency, and Σ is the disk surface density. We shall assume hereafter that the dynamics of the HI disk of NGC 2915 can be adequately modeled with an isothermal gas in which the sound speed c_s is equal everywhere to the observed velocity dispersion: $c_s \equiv \sigma_v$. A look at Eq. (1) informs us that once Ω_p is chosen, the value for k (and therefore for k_r) is imposed, since Ω, κ, Σ and c_s are imposed by the observations. More precisely, k is given by a second-order polynomial

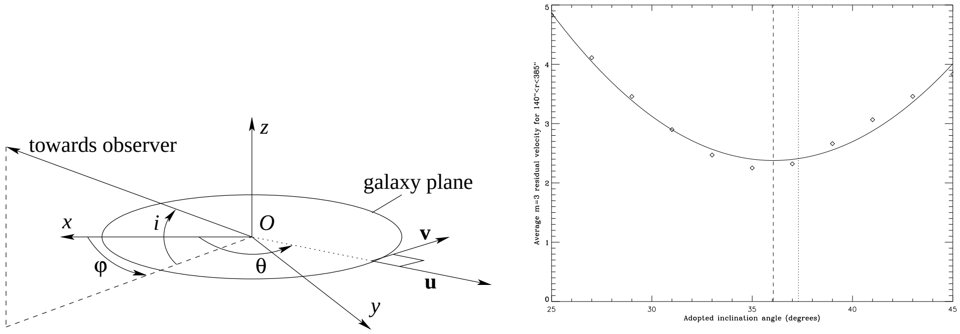

Figure 2. a *(left)*: sketch of the notations used in text. b *(right)*: average amplitude of the $m = 3$ deprojected radial velocity map (average between 140 and 385 arc-seconds), as a function of the galaxy assumed inclination.

equation, which admits two roots, corresponding respectively to the so-called long and short wave. Note that in the regime where Q is high (i.e. when the term $-2\pi G\Sigma|k|$ is negligible compared to the two others), these two roots are very close to each other, and one can in fact consider only the short wave. The value of k_r is linked to the pitch-angle β of the spiral pattern by:

$$\tan\beta = \frac{m}{k_r r} \tag{2}$$

Therefore, one can conclude from Eqs. (1) and (2) that, given the observational constraints, a guess of the pattern frequency Ω_p of the perturber (and therefore of the wave, in a forced regime) leads to a value for the spiral pattern pitch angle. One needs therefore to adjust the perturber frequency so as to match the observed pitch angle. This latter can be estimated by $\tan\phi_{\rm obs} = \frac{d\log r}{d\theta}$ (where θ is the azimuthal angle) on a deprojected map of the galaxy, and it turns out to amount to $\phi_{\rm obs} = 7 - 10°$.

In the linear regime, the wave amplitude (which does not appear in the dispersion relation) is independent of its pitch-angle, which means that one can successively adjust the perturber pattern frequency and then its strength so as to match respectively the spiral pattern pitch-angle and then its arm-interarm contrast. In our situation however the arm-interarm contrast is not small compared to unity, the disk response is non-linear and one cannot find the perturber parameters (Ω_p and strength) simply by exploring independently the wave pitch-angle and arm-interarm contrast. This is one of the reasons why this parameter fit needs to be undertaken through numerical simulations. It should also be noted that most of the torque from the perturbing potential is received by the disk at the Inner and Outer Lindblad resonance, i.e. when $\Omega(r) = \Omega_p \pm \frac{\kappa}{m}$. Therefore, the shape of the radial profile of the perturbing potential should one have a minor impact on the disk response. This of course greatly simplifies the parameter space exploration, as one can adopt any crude prescription for

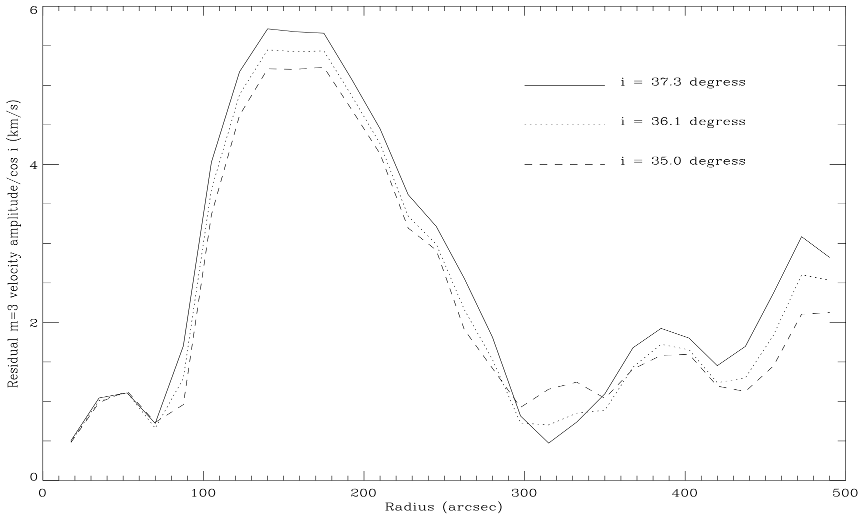

Figure 3. This figure shows the radial behavior of the amplitude of the $m = 3$ component of the deprojected radial velocity map (corrected from $\cos i$), for three different values of the assumed galactic plane inclination.

the perturber shape and simply adjust its strength by an adequate scaling (e.g. scaling the mass of a bar-like perturber, or the triaxiality of a triaxial halo). On the other hand, it may hinder any attempt to reach a detailed knowledge of the perturber, as it prevents one from disentangling various satisfactory fits of the disk response.

2.2. A suitable velocity constraint

Prerequisite If one denotes by u and v the radial and azimuthal velocity component of the gas flow in the *galactocentric* frame, than the radial velocity field of the material w.r.t. the observer can be expressed as:

$$v_r = [-u\cos(\theta-\varphi) + v\sin(\theta-\varphi)]\cos i \tag{3}$$

where the notations are explicited at Fig. 2a. As the perturbed velocity field (u, v) associated to an m-folded spiral density wave has an $e^{im\theta}$ dependence in azimuth, one can easily see from Eq. (3) that it will lead to an $m-1$ and $m+1$ folded signature in the deprojected radial velocity map. This signature can in principle be used to constrain the models, in a way explicited below.

Case of an $m = 2$ spiral density wave From the above the perturbed velocity field associated to an $m = 2$ spiral will have an $m = 1$ and $m = 3$ signature on the deprojected radial velocity map.

Case of the $m = 1$ component The $m = 1$ component can come on one hand from the $m = 2$ spiral density wave perturbed velocity field, but also from the

$m = 0$ component of the velocity field (i.e. the unperturbed circular rotation of the galactic disk). As soon as the inclination of the disk varies with radius (i.e. as soon as the disk is warped) it is not possible to disentangle which part of the $m = 1$ deprojected radial velocity comes from the $m = 2$ density wave and which part comes from the warp (this corresponds to the infamous bias introduced in warps tilted ring model fits by the so-called streaming motions, i.e. horizontal $m = 2$ perturbed velocity fields). As there are indications that the disk of NGC 2915 may be slightly warped (MCBF), we do not consider the $m = 1$ component of the radial velocity deprojected map as a suitable constraint for the simulations, and we rather focus on the $m = 3$ component.

Case of the $m = 3$ component The $m = 3$ component of the deprojected radial velocity map can come from an $m = 2$ spiral density wave (as well as from a $m = 4$ density wave, which has $m = 3$ and $m = 5$ signatures). It can also come (see also Teuben, these proceedings, and ref. therein) from a wrong evaluation of the galactic plane inclination. An error Δi on the galactic plane inclination will of course lead to a $O(\Delta i)$ $m = 1$ residual (one blue side and one red side), but also to a weak $O(\Delta i^2)$ $m = 3$ residual. Although the $m = 3$ which comes from the inclination error is weak ($\sim V_{\rm rot}\Delta i^2$), it is important to compare it with the $m = 3$ residual which comes from the bar/spiral, which has also a small value. Fig. 2b shows the radius averaged value of this component as a function of the assumed inclination for the disk of NGC 2915. The solid line shows a second order polynomial fit to the data points. One can easily check that the parabola fit scales as $\Delta i^2 V_{\rm rot}$, as expected. Fig. 3 shows the $m = 3$ deprojected radial velocity field amplitude for three special values of the assumed inclination: 35° (corresponding to the lowest data point), 36.1° (corresponding to the fit minimum), and 37.3° (which corresponds to the inclination inferred from an elliptical fit of the outermost column density isocontours of the disk of NGC 2915). These profiles do not markedly differ from each other, which shows that the (small) uncertainty we have on the disk inclination has little impact on the radial profile of the amplitude of the $m = 3$ deprojected radial velocity component (we shall call this profile $\tilde{V}_3^{\rm obs}(r)$ hereafter). A warp could affect this profile in a way similar to the uncertainty on the inclination, but again its impact on the profile shape would be mild. Therefore we consider the radial profile $\tilde{V}_3^{\rm obs}(r)$ as a suitable constraint for the simulations. It is taken into account as follows: we define the following scalar product between two radial functions f and g:

$$\langle f|g\rangle = \int_0^{r_{\rm ext}} r f(r) g(r) dr \tag{4}$$

We then search the maximum value over a run of:

$$\chi = \frac{\langle \tilde{V}_3^{\rm obs}(r)|\tilde{V}_3^{\rm sim}(r)\rangle}{[\langle \tilde{V}_3^{\rm obs}(r)|\tilde{V}_3^{\rm obs}(r)\rangle\langle \tilde{V}_3^{\rm sim}(r)|\tilde{V}_3^{\rm sim}(r)\rangle]^{\frac{1}{2}}} \tag{5}$$

varying both the time and φ (the observer azimuth) as $\tilde{V}_3(r)$ depends on φ. By construction, $|\chi|$ is always smaller than one, and is one if $\tilde{V}_3^{\rm obs}(r)$ and $\tilde{V}_3^{\rm sim}(r)$ are proportional (Schwarz's theorem). The closer $|\chi|$ is to one, the more $\tilde{V}_3^{\rm obs}(r)$

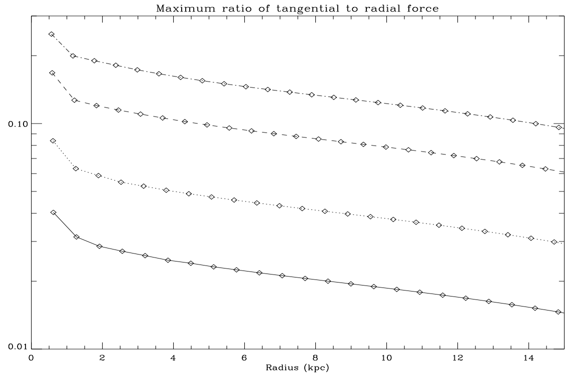

Figure 4. This figure shows the radial profile of the tangential to radial acceleration ratio for four different triaxial halos, with $b/a =$ 0.95, 0.9, 0.8 and 0.7. All of these halos have $c/a = 1$. Each halo in this sample has a core radius $r_c = 2$ kpc.

and $\tilde{V}_3^{\rm sim}(r)$ "look alike". In the linear regime there is an obvious advantage in using this procedure: χ does not depend on the amplitude of the perturbing potential, which can therefore be adapted in a second step so as to match $\tilde{V}_3^{\rm obs}(r)$ both in shape and absolute value. Note also that the r-weighting in the scalar product expression corresponds to a uniform weighting of the 2D deprojected map.

At this point we have outlined how to take into account the constraints arising from the zero$^{\rm th}$ and first moment (i.e. column density and velocity field) of the observation data cube. The second moment, i.e. the dispersion velocity, is directly imposed to the model as the sound speed.

3. Description of the hydrocode

The code we have used is a simple 2D Eulerian finite difference hydrocode, on a polar mesh. The advection is based on a second order upstream difference. There is no energy equation, as the closure relation is provided by the observed dispersion velocity (treated here as the sound speed). This ensures that at any instant in time the simulated disk has a sound speed which coincides with the observed velocity dispersion. The drawback is that at low Q parameter, the disk quickly fragments into clumps. This is not the case in our externally forced disk cases however. Since beam smearing effects overestimate the dispersion near the center, several profiles have been tried in which central values of σ_v were lower than the ones observed. Azimuthal advection was treated so as to get rid of the average azimuthal velocity at each radius in order to relieve the Courant condition and increase the timestep. The gain in using such a modified advection algorithm is relatively small however in our case since we have to deal with strong radial streaming at the center where the disk response is bar-like. As we use a 2D code, we neglect the warping of the disk of NGC 2915. The external forcing is provided either by a bar or by a triaxial halo. The bar is

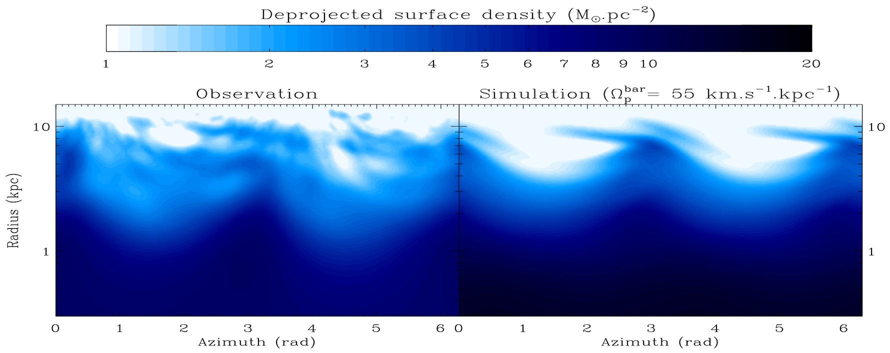

Figure 5. This figure compares the deprojected surface density of NGC 2915 (left) and of the best fit in which the disk response is triggered by an external bar-like potential. One can see that the pitch angle and angular extent of the spiral arms is about the same in both cases.

characterized by its pattern speed Ω_p and by a surface density:

$$\Sigma(x,y) = \Sigma_b \left[\left(x^n + y^n \frac{a^n}{b^n} \right)^{\frac{1}{n}} \right] \tag{6}$$

where x (resp. y) is measured along the bar major (resp. minor) axis, b/a is the bar axis ratio, $\Sigma_b(r)$ is the bar density profile along the bar major axis, and n is a dimensionless index which characterizes the bar surface density isocontours shape. A triaxial halo is characterized by its pattern speed Ω_p and by the maximum ratio of the tangential to radial acceleration of a test particle. The tangential acceleration has a $m = 2$ dependence on azimuth. The acceleration ratio was chosen either constant in radius, or with a dependence such as the one depicted at Fig. 4.

Self-gravity is taken into account. The disk potential is evaluated through FFTs. Although potential evaluation with this technique is known to be affected by numerical artifacts, we feel that due to the weakness of self-gravity effects in our case, it is safe to use such a fast evaluation.

4. Results and discussion

Due to space constraints we shall not present the simulation results comprehensively here, but we rather present the best fits that could be obtained. The whole set of results will be presented elsewhere (Masset & Bureau, in prep.). Fig. 5 shows the disk surface density in the $(\theta, \log r)$ plane, as observed and in a simulation in which the forcing potential is provided by a bar which has the following

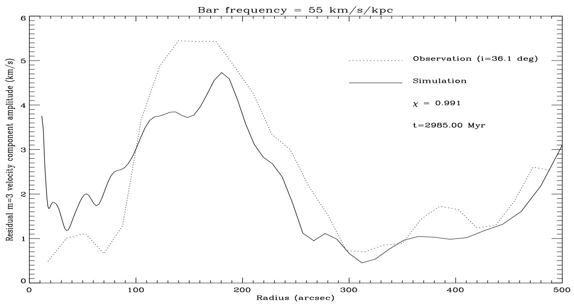

Figure 6. $\tilde{V}_3^{\rm obs}(r)$ (dotted line) and $\tilde{V}_3^{\rm sim}(r)$ (solid line).

characteristics: $\Omega_p = 55$ km/s/kpc, $b/a = 0.4$, $n = 4$, $M_{\rm bar} = 1.2 \cdot 10^9\ M_\odot$, and the bar density profile along the major axis is exponential with a length-scale $R_b = 4$ kpc. This is obviously a very crude description of a bar, but as has already been stressed out, the radial profile of the perturbing potential is of minor importance in this problem. Fig. 6 shows the comparison between $\tilde{V}_3^{\rm obs}(r)$ and $\tilde{V}_3^{\rm sim}(r)$. The time at which this maximum value for χ is reached is about 3 Gyr, much longer than the relaxation time over which the disk initially exhibits transient features.

One can note that the disk response is much better accounted for by the model in the outer disk than in the inner disk. The reason for that is our poor knowledge of the velocity dispersion in the inner region, as beam smearing effects tend to overestimate this latter. Satisfactory fits are produced as well for the surface density for $\Omega_p = 50$ and $\Omega_p = 60$ km/s/kpc, and for the $m = 3$ component of the deprojected radial velocity for $\Omega_p = 60$ km/s/kpc, for which a comparable value of the correlation coefficient χ is reached. Models with a triaxial halo also lead to satisfactory fits for the velocity residuals for this range of pattern frequencies, but with lower χ coefficient and not so satisfactory density response fits. The horizontal axis ratio needed to account for the $m = 3$ velocity residual amplitude and arm-interarm contrast would be about $b/a \sim 0.8$ (with c/a assumed to be one).

The fact that the same perturber strength can simultaneously account for the arm-interarm contrast and $\tilde{V}_3(r)$ profile amplitude gives us additional confidence in the validity of our models and is a strong point in favor of an external driving of the observed spiral structure. The mass of the optical counterpart of NGC 2915 is too small to represent the bar-like perturber, and in any case the spiral structure would be excited by an *unseen* component. The pattern frequency range inferred from the models is compatible with the lower limit determined by Bureau et al. 1999.

References

Bureau, M., Freeman, K.C. and Meurer, G.R. 1999 AJ, 118, 2158

Meurer, G.R., Mackie, G. and Carignan, C. 1994, AJ, 107, 202

Meurer, G.R., Carignan, C., Beaulieu, S.F., and Freeman, K.C. 1996, AJ, 111, 155